



The Coupling and Evolution of Kelvin–Helmholtz and Rayleigh–Taylor Instabilities in the Heliosheath

Xiaohan Ma^{ID}, Merav Opher^{ID}, and Marc Kornbleuth^{ID}

Boston University, USA

Received 2025 April 28; revised 2025 June 12; accepted 2025 June 24; published 2025 July 29

Abstract

The shape and structure of the heliosphere remain subjects of ongoing debate, with current models differing on how far the heliospheric jets that form the two-lobe structure extend down the heliotail and whether the surrounding interstellar medium can penetrate the region between the lobes. Rayleigh–Taylor (RT) and Kelvin–Helmholtz (KH) instabilities along the axis of the heliospheric jets have been proposed as key drivers of turbulence in the heliosheath (HS). In this work, we present results from 225 yr MHD simulations that reveal periodic variations in solar wind speed and magnetic field within the HS, coinciding with the cyclic growth of RT and KH instabilities. At the onset of each cycle, the instabilities initially develop simultaneously in the direction normal to the plane of the heliospheric jet, with an average timescale of ~ 4.2 yr. As the system evolves over ~ 11.1 yr, RT and KH modes decouple, with KH modes subsequently dominating beyond the high-density region and leading to a reduced growth rate, corresponding to a timescale of ~ 12.9 yr. These findings suggest that RT and KH instabilities can coevolve and reoccur periodically, contributing to turbulence generation in the HS. Their nonlinear development may play a fundamental role in shaping the large-scale structure of the heliosphere, particularly in the formation and evolution of the open heliospheric tail.

Unified Astronomy Thesaurus concepts: [Heliosphere \(711\)](#); [Magnetohydrodynamics \(1964\)](#); [Hydrodynamics \(1963\)](#); [Solar wind \(1534\)](#)

1. Introduction

Understanding the dynamics of the heliosphere—the vast region surrounding the Sun where the solar wind interacts with the interstellar medium (ISM)—is crucial for resolving ongoing debates about its structure. Early models of the heliosphere depicted the heliosphere as having a comet-like shape with an extended tail (E. N. Parker 1961; V. B. Baranov et al. 1976). However, more recent studies suggest that the heliosphere may have a short split-tail structure (J. F. Drake et al. 2015; M. Opher et al. 2015; M. Opher et al. 2020). Studies suggest that the tension in the solar magnetic field plays a crucial role in shaping solar wind dynamics within the heliosheath (HS). The spiral structure of the solar magnetic field deflects solar wind flows, preventing them from stretching out and instead confining them into two distinct lobes, known as heliospheric jets (G. Yu 1974; J. F. Drake et al. 2015; V. Izmodenov & D. Alexashov 2015; M. Opher et al. 2015; N. V. Pogorelov et al. 2015; E. A. Golikov et al. 2016; M. Kornbleuth et al. 2021).

However, existing models differ in their predictions regarding the spatial extent of the heliospheric jets and the ability of the surrounding interstellar medium (ISM) to penetrate the region between the lobes. Instabilities within the heliosheath (HS) affect solar wind flows, drive turbulence, and influence the transport of energetic particles. These instabilities play a crucial role in shaping the large-scale structure of the heliosphere, particularly in its tail region, where they govern the mixing and reconnection of solar and interstellar plasmas. Understanding these processes is essential

for explaining the formation and evolution of the split-tail structure.

Early studies predominantly focused on instabilities at the heliopause (HP). The Rayleigh–Taylor (RT)-like instability, driven by the effective gravity generated by charge-exchange interactions between neutral hydrogen atoms and plasma ions, has been extensively studied (P. Liewer et al. 1996; G. P. Zank et al. 1996; G. P. Zank 1999). This instability is particularly significant because the ISM plasma is much denser than the solar wind, leading to unstable interfaces where the denser ISM pushes into the less dense solar wind plasma. Studies have further explored the stabilizing effects of hot HS neutrals on this process (V. Florinski et al. 2005; K. Avinash et al. 2014).

In addition to RT instability, Kelvin–Helmholtz (KH) instability develops due to velocity shear at the HP, where differential motion between the solar wind and the ISM can generate wavelike perturbations along the boundary (V. Baranov et al. 1992; S. V. Chalov 1996; K. Avinash et al. 2015). KH instabilities are particularly prominent along the flanks of the HP, where they depend on the perturbation wavevector orientation and the density contrast across the boundary (V. Baranov et al. 1992). Moreover, short-wavelength disturbances can destabilize the nose of the HP, further modifying its shape over time (S. V. Chalov 1996).

Inside the HS, the interaction between neutral hydrogen atoms from the ISM and ionized solar wind plasma introduces instability mechanisms as well. While kink instabilities have been proposed as key drivers of turbulence in astrophysical jets (M. C. Begelman 1998) and suggested to influence the heliospheric tail (N. V. Pogorelov et al. 2015; F. Fraternale et al. 2023), recent studies indicate that the heliospheric jets may be stabilized by their magnetic field structure and velocity shear, suppressing kink or sausage instabilities (M. Opher et al. 2021).



Original content from this work may be used under the terms of the [Creative Commons Attribution 4.0 licence](#). Any further distribution of this work must maintain attribution to the author(s) and the title of the work, journal citation and DOI.

Instead, M. Opher et al. (2021) identified a Rayleigh–Taylor-like instability along the axis of the heliospheric jets, driven by charge-exchange interactions between neutral hydrogen atoms and solar wind ions, which generates an effective gravitational force, leading to a perpendicular density gradient that facilitates the instability. The estimated growth timescale of this instability was estimated to be years, depending on the ISM neutral hydrogen density.

Beyond Rayleigh–Taylor instabilities, velocity shear inside the HS can trigger KH instabilities. X. Ma et al. (2024) found that a low-speed solar wind region exists within the HS, formed due to charge exchange and magnetic tension around the axis of the heliospheric jets. The resulting shear flow leads to the onset of KH instabilities, with an estimated growth timescale of 5–7 yr based on simulation results. In addition, as compared to the dynamic time of instabilities, the low-speed region allows sufficient time for instabilities to develop.

Understanding the development and interplay of these instabilities within the HS is essential for comprehending the dynamical processes governing the heliosphere’s large-scale structure. These instabilities influence turbulence and the interaction between solar and interstellar plasmas, ultimately shaping the structure of the heliospheric tail. In this paper, we examined the coupling and evolution of KH and RT instabilities inside the HS with long-time variation.

This paper is organized as follows: We describe the magnetohydrodynamic (MHD) model and IMS conditions used for the simulations in Section 2. Section 3 discusses the periodic development of the RT and KH instabilities in the HS with a long revolution time. Finally, in Section 4 we present discussions about how variations in neutral hydrogen density, velocity shear, and magnetic field structure influence the growth of RT and KH and their coupling mechanisms.

2. Numerical Model

The MHD model of the Outer Heliosphere (OH) components uses the Space Weather Modeling Framework (SWMF; G. Tóth et al. 2012), which includes the Block-Adaptive Tree Solar wind Roe-Type Upwind Scheme (BATS-R-US) solver (G. Tóth et al. 2012). BATS-R-US is a 3D block-adaptive, upwind finite-volume MHD code designed for both steady-state and time-dependent simulations. It uses various time-stepping algorithms, including local time stepping, which accelerates convergence to steady-state solutions by assigning time steps based on local stability conditions and time-accurate simulations, which use a uniform time step across all grid cells (G. Tóth et al. 2012).

M. Opher et al. (2003) adapted the BATS-R-US code to model the outer heliosphere (OH) as part of the OH component within SWMF. This component has since been extended to include multiple ion fluids (M. Opher et al. 2020) and multiple neutral fluids (M. Opher et al. 2009). Meanwhile, a kinetic-MHD version of the model has been developed to describe neutral hydrogen atoms kinetically (A. T. Michael et al. 2022; Y. Chen et al. 2024). In this work, we adopt a single-ion fluid approach, following the methodology of M. Opher et al. (2015, 2021), in which the cold thermal solar wind and hot pickup ions (PUIs) are treated as a single-fluid species (G. P. Zank 1999). The neutral hydrogen is modeled using a four-fluid approximation, as described by G. P. Zank (1999), M. Opher et al. (2009). The simulation employs a coordinate

system where the z -axis aligns with the solar rotation axis. The interstellar flow lies in the x – z plane, tilted 5° above the x -axis, which defines the direction of the x -axis. The y -axis completes the right-handed coordinate system.

The inner boundary of our simulation domain is set at a sphere located at 30 au. At this boundary, the solar wind parameters are: $U_{\text{SW}} = 417 \text{ km s}^{-1}$, $n_{\text{SW}} = 8.74 \times 10^{-3} \text{ cm}^{-3}$, and $T_{\text{SW}} = 1.087 \times 10^5 \text{ K}$. For the solar wind’s magnetic field, we use the Parker spiral model (E. N. Parker 1958), with $B_{\text{SW}} = 7.17 \times 10^{-3} \text{ nT}$ at the equator. To minimize artificial reconnection effects, we adopt a monopole configuration for the solar magnetic field, aligned with the solar rotation axis, as done in M. Opher et al. (2015). The solar wind flow at the inner boundary is assumed to be spherically symmetric. The ISM parameters are the same as in M. Opher et al. (2015), with $v_{\text{ISM}} = 26.4 \text{ km s}^{-1}$, $n_{\text{ISM}} = 0.06 \text{ cm}^{-3}$, and $T_{\text{ISM}} = 6519 \text{ K}$. The hydrogen atom number density in the ISM is $n_{\text{H}} = 0.18 \text{ cm}^{-3}$.

The interstellar magnetic field (ISM) in the model is given by $B_{\text{ISM}} = 4.4 \mu\text{G} = 0.44 \text{ nT}$. X. Ma et al. (2024) use an ideal ISM condition with the magnetic field of ISM only in the z -direction. In this model, we adopt a realistic ISM condition, with the direction of the interstellar magnetic field (\mathbf{B}_{ISM}) to lie within the hydrogen deflection plane, characterized by ecliptic coordinates of latitude -18.4° and longitude 67.8° , and offset by 20° from the direction of the interstellar wind (\mathbf{V}_{ISM}) (M. Opher et al. 2015).

To minimize the impact of initial numerical transients on the instability analysis, we adopt the same grid resolution as X. Ma et al. (2024). The simulation begins with a coarse grid. Around the termination shock (TS), the cell size is set to 12 au, which can damp any initial numerical instability inside the HS. The coarse grid resolution precludes the development of instabilities. It runs without charge exchange using local time stepping for 30,000 steps. It then transitions to accurate time stepping and continues for 50 yr until reaching a steady state. At this point, we turned on and ran the simulation for an additional 500 yr to ensure the heliosphere fully stabilizes. During this period, a low-speed solar wind region develops inside the heliosheath, as described in X. Ma et al. (2024). We reduced the grid size to approximately 2 au inside the HS. Before the grid refinement, initial numerical transients had already completed the evolution and dissipated, while the heliosphere had achieved a steady state. After the grid was refined, the development of instabilities in the HS can appear in the model results.

To minimize the impact of numerical transients on the instability analysis, we follow the grid resolution strategy of X. Ma et al. (2024). The simulation begins with a coarse grid, with a cell size of 12 au in the HS, which suppresses early numerical instabilities. It runs without charge exchange using local time stepping for 30,000 steps, followed by accurate time stepping for 50 yr until a steady state is reached. Charge exchange is then turned on, and the simulation continues for another 500 yr to allow the heliosphere to achieve a steady state, during which a low-speed solar wind region forms in the HS (X. Ma et al. 2024). After stabilization, the grid is refined to ~ 2 au inside the HS. At this point, initial transients have dissipated, and the heliosphere has reached a steady state, allowing instabilities to develop in the model.

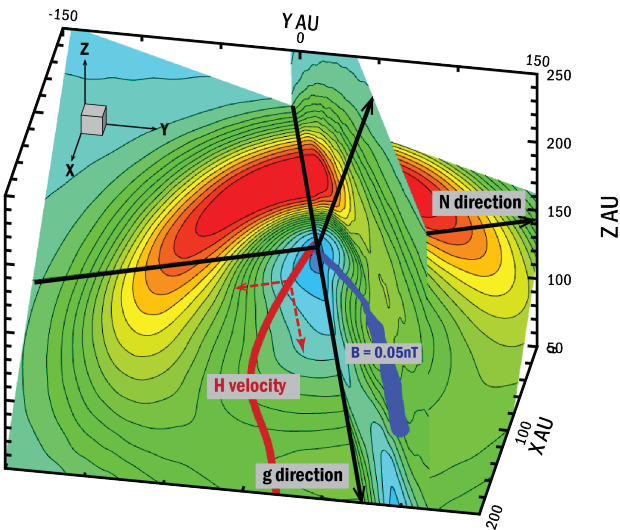


Figure 1. The coordinates defined to describe the instabilities in the HS. The color contour shows the solar wind speed. The blue isosurface corresponds to $B = 0.05$ nT, marking the axis of the heliospheric jet. The slice aligned with the jet axis defines the plane of the heliospheric jet. The g -direction lies in this plane and indicates the growth direction of the instability. The N -direction is perpendicular to the plane of the jet, corresponding to another growth direction of the instability. The other slice is perpendicular to the jet axis, with streamlines of neutral hydrogen (H) in red. The red dashed lines indicate components along both the g - and N -directions.

3. Result

Due to the heliospheric jet axis not being along the meridional plane but having an angle with the direction of neutral H velocity (as shown in Figure 1), the effective gravity arising from charge exchange between neutral H atoms and solar wind ions, as described in M. Opher et al. (2021), deviates from the plane of the heliospheric jet. As shown in Figure 1, g -direction represents the growth direction of the instability in the plane of the heliospheric jet, and N -direction aligns the growth direction of the instability perpendicular to the plane of the heliospheric jet. The effective gravity has both components along the g -direction and N -direction, further facilitating RT instabilities (M. Opher et al. 2021) in both directions, adding to the complexity of instability development within the HS.

Figure 2 presents the plasma variations over 225 yr of evolution after grid refinement. Panel (A) shows the temporal variation of the solar wind speed at the location marked by a red circle in panel (B), revealing periodic fluctuations rather than a constant value. To analyze these variations, we selected eight representative time points: 3, 24, 42, 51, 110, 118, 194, and 208 yr after grid refinement, corresponding to the peak and valley values of the solar wind speed. In panels (B–D), the figures labeled with numbers 1–8 correspond to the periods indicated by the dashed lines in (A), showing color contours of the solar wind speed, magnetic field, and density in the plane of the heliospheric jet. These results provide insight into the dynamic evolution of the solar wind parameters over time inside the HS.

As shown in panels (B1–8), the structure of the low-speed region varies over time. X. Ma et al. (2024) illustrated that the shear flow formed in the low-speed region within the HS leads to the KH instability. Therefore, the time variation of the low-speed region can influence the development of KH instability.

To present the periodical variation clearly, we present the solar wind velocity at the same location (marked by a red circle) in panel (A). Furthermore, as shown in panel (C), the axis of the heliospheric jet, defined by $B < 0.05$ nT, also varies over time, transitioning from an initially continuous structure in the jet panel to multiple discrete ringlike regions. Along the axis, the density of solar wind is higher than around. The high-density solar wind region, which initially forms a continuous jet extending from the TS to the heliotail, transforms into a series of discontinuous, near-ring-like structures as shown in panels (D1–8). As we will show below, these are not discontinuous structures, but rather the result of a 3D motion of the heliospheric jet axis.

Figure 3 presents the 3D results corresponding to the eight periods in Figure 2 (i.e., 3, 24, 42, 51, 110, 118, 194, and 208 yr after grid refinement), further revealing the dynamical processes within the HS induced by instabilities. The white isosurface in the figure represents $B = 0.05$ nT, marking the axis of the heliospheric jet, while the slice corresponds to the jet panel, displaying the contour of the magnetic field strength as shown in Figure 2 panels (C1–8). The heliospheric jet axis periodically crosses the jet panel, leaving multiple discrete ringlike regions in the jet panel, as shown in Figure 2 panels (C1–C8). The periodically in-and-out structure of the magnetic field is due to the instabilities within the HS that periodically develop near the TS and propagate toward the heliotail.

As instabilities in the HS occur periodically, the growth rate for each cycle can be estimated by tracking the displacement (D) of the heliospheric jet axis in the g - and N -directions over time. Figure 4 presents cases where the initial times $t_0 = 3, 63$, and 102 yr after grid refinement, illustrating the displacement of instability structures in the g -direction (in). Figure 5 shows similar cases with initial times $t_0 = 3, 66$, and 104 yr, depicting the displacement of instability structures in the N -direction (as indicated before). In both figures, displacements are shown at times $t_0, t - t_0 = 6, 12$, and 18 yr within the respective instability cycles.

The time evolution of displacement in both the g - and N -directions over 225 yr after grid refinement is shown in Figure 6. In Figure 6(1), for each instability cycle in the g -direction, the displacement D follows an exponential growth relationship with $t - t_0$, where t_0 represents the initial time of each cycle. The instability growth rate perpendicular to the heliospheric jet axis (in the N -direction) is estimated from the linear fit of the logarithm of displacement, $\ln(D)$, versus $t - t_0$. Table 1 presents the fitted growth rate γ for each cycle along with its corresponding timescale $1/\gamma$.

For the three cases in Figure 4, the exponential fit of displacement yields a growth rate of $\gamma = 0.175$ for $t_0 = 3$ yr with a correlation coefficient of $R^2 = 0.99$, corresponding to a timescale of $1/\gamma = 5.7$ yr. For $t_0 = 63$ yr, the growth rate is $\gamma = 0.172$ with $R^2 = 0.98$, giving a timescale of $1/\gamma = 5.8$ yr. For $t_0 = 102$ yr, the growth rate is $\gamma = 0.123$ with $R^2 = 0.94$, resulting in a timescale of $1/\gamma = 8.1$ yr. For these nine instability cycles, the average growth rate is $\gamma = 0.169$, corresponding to a timescale of $1/\gamma = 5.9$ yr.

In Figure 6(2), each instability cycle in the N -direction (in the plane perpendicular to the plane of the heliospheric jet) exhibits a turning point in the relationship between $\ln(d)$ and $(t - t_0)$. This turning point is identified by analyzing changes in the slope of the $\ln(d)$ versus $t - t_0$ curve. The turning point is identified as the time at which a significant change occurs in

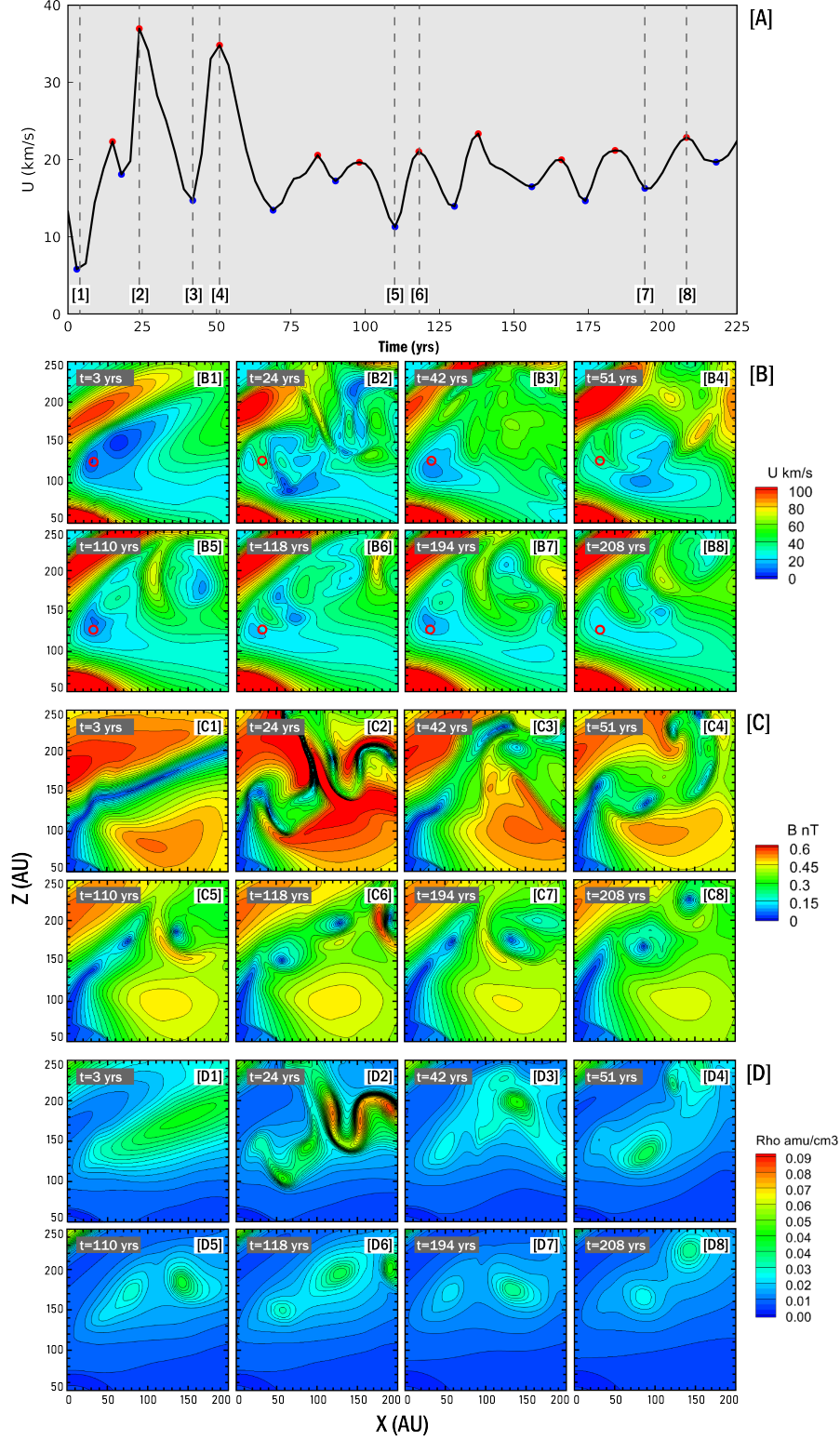


Figure 2. Model results for 225 yr after grid refinement. (A) Solar wind speed probed at the point marked in a red circle in panel (B). (B–D) show the contours of solar wind speed (B), magnetic field (C), and density (D) in the plane of the heliospheric jet, at eight periods: 3, 24, 42, 51, 110, 118, 194, and 208 yr after grid refinement.

the local slope between adjacent data points. The slope of the $\ln(d)$ versus $t - t_0$ curve differs before and after the turning point in each cycle, indicating that the displacement d adheres to a power-law relationship with $t - t_0$ but with distinct growth

rates at different stages of the cycle. Table 2 summarizes the fitted instability growth rates (γ) and corresponding timescales ($1/\gamma$) before and after the turning point in each cycle. The average timescale before the turning point is 4.2 yr. The mean

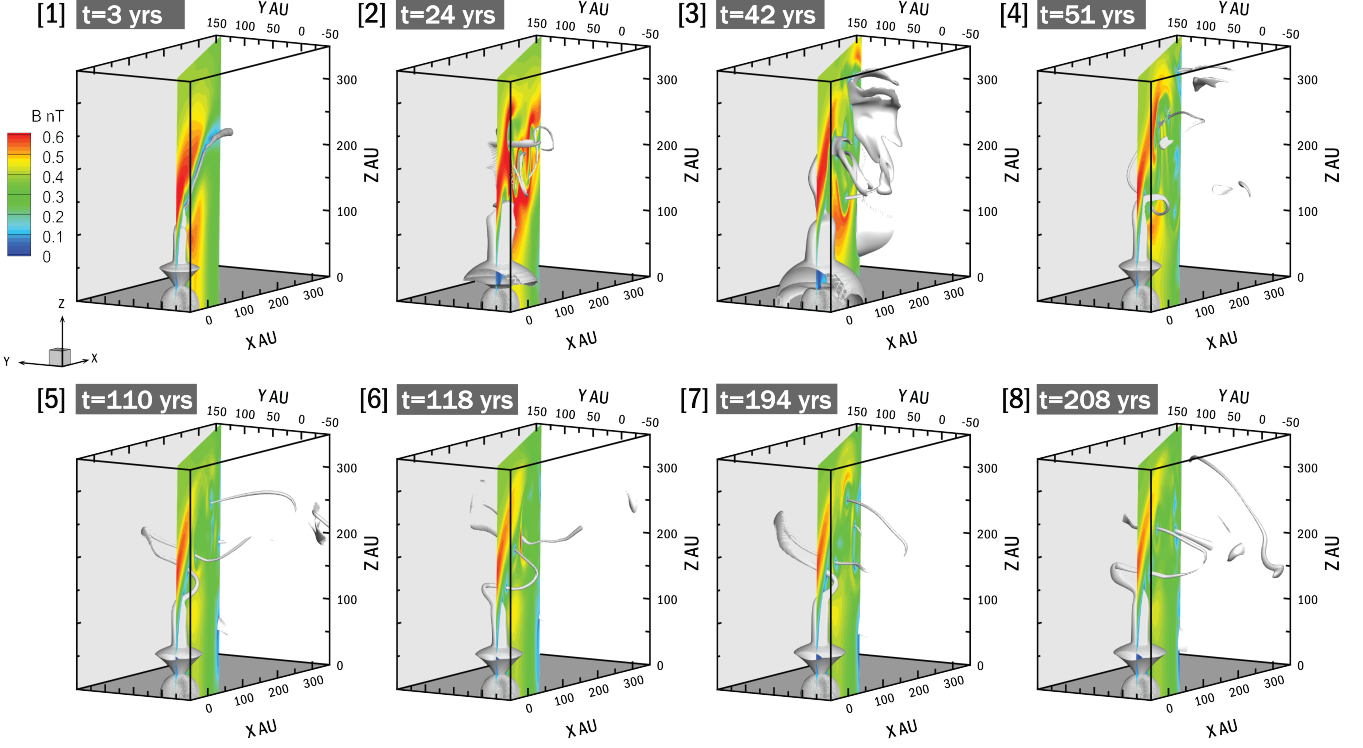


Figure 3. The 3D structure of the heliospheric jet axis, with white isosurfaces marking $B = 0.05$ nT at eight periods: 3, 24, 42, 51, 110, 118, 194, and 208 yr after grid refinement. The slices represent the plane of the heliospheric jets, showing the contour of B as in Figure 2, Panels (C1–8).

time to reach the turning point is 11.1 yr, and the average timescale after the turning point increases to 12.9 yr. This transition is characterized by a significant reduction in the growth rate, indicating a change in the underlying instability growth mechanism.

For the three cases in Figure 5, the exponential fit of displacement yields a growth rate of $\gamma = 0.250$ for $t_0 = 3$ yr ($R^2 = 0.96$), corresponding to a timescale of $1/\gamma = 4.0$ yr. After the turning point at $t_1 = 18$ yr, the growth rate decreases to $\gamma = 0.091$ ($R^2 = 0.98$), with a timescale of $1/\gamma = 11.0$ yr. For $t_0 = 66$ yr, the growth rate is $\gamma = 0.189$ ($R^2 = 0.98$), corresponding to a timescale of $1/\gamma = 5.3$ yr. After the turning point at $t_1 = 72$ yr, it drops to $\gamma = 0.090$ ($R^2 = 1.00$), with a timescale of $1/\gamma = 11.1$ yr. For $t_0 = 104$ yr, the growth rate is $\gamma = 0.238$ ($R^2 = 0.96$), yielding a timescale of $1/\gamma = 4.2$ yr. Following the turning point at $t_1 = 112$ yr, it declines to $\gamma = 0.079$ ($R^2 = 0.99$), with a timescale of $1/\gamma = 12.7$ yr. For all nine instability cycles, the average growth rate before the turning point is $\gamma = 0.234$ ($1/\gamma = 4.2$ yr), while after the turning point, it decreases to $\gamma = 0.077$ ($1/\gamma = 12.9$ yr).

To estimate growth rate of instability in both g - and N -direction and better understand the physical reason for the turning point in instability growth rate in N -direction, we made a cross section perpendicular to the axis at the initial time of instability which is $t = 3$ yr and $t = 66$ yr and at the turning point time which is $t = 18$ yr and $t = 72$ yr as shown in Figure 7. Figure 7(A1–4) presents the total solar wind speed in the cross-sectional view perpendicular to the heliospheric jet. Figure 7(B1–4) presents solar wind density, total speed, speed along the g -direction, and neutral hydrogen speed along the g -direction along the line cut in the g -direction. While Figures 7(C1–4) present similar parameters along the line cut in the N -direction. These parameters can be used to

estimate the theoretical growth rate of RT instability and KH instability in both g - and N -directions.

As described in M. Opher et al. (2021), the growth rate of the Rayleigh–Taylor instability (γ_{RTI}) for a slab of width A with high-density ρ_i , surrounded by two regions of lower density ρ_o , as shown in Figure 7(B), can be expressed as:

$$\gamma_{\text{RTI}} = \sqrt{\alpha \cdot k_{\text{RTI}} \cdot g^*}$$
, where $\alpha = \sqrt{\frac{T_k(\rho_i / \rho_o - 1)^2}{(\rho_i / \rho_o + T_k)(\rho_i / \rho_o T_k + 1)}}$ is a dimensionless parameter that describes the instability's response to density gradients. Here, i and o represent the inside and outside of the slab, respectively, and $T_k = \tanh\left(\frac{k_{\text{RTI}} A}{2}\right)$, where k_{RTI} is RT instability wavenumber, $k_{\text{RTI}} = \frac{2\pi}{\lambda}$, $\lambda = 107$ au = 0.0587 au $^{-1}$ is the wavelength of the perturbation along the jet. The half-peak width A can be estimated from the distance between the green dashed lines shown in Figure 7. The effective gravitational acceleration $g^* = \nu_{\text{CN}} \Delta v_{\text{HP}}$, where $\Delta v_{\text{HP}} = v_H - v_p$ and $\nu_{\text{CN}} = \sigma n_H U^*$ is the charge-exchange frequency, where $\sigma = 2.46 \times 10^{-15}$ cm 2 is the charge-exchange cross section (B. Lindsay & R. Stebbings 2005) and $U^* = 200$ km s $^{-1}$ is the effective velocity difference as described in M. Opher et al. (2021) and $n_H = 0.18$ cm $^{-3}$ is the neutral density of ISM as described in Section 2. For the first cycle of instability shown in Figure 7 (B1), $A = 47.8$ au, so $T_k = 0.9$, and $\Delta v_{\text{HP}} = v_H - v_p$ in g -direction is ~ 12.9 km s $^{-1}$, $\rho_i / \rho_o = 3.45$, so RT instability growth rate is $\gamma_{\text{RTI}} = 0.156$ and growth timescale is $1/\gamma_{\text{RTI}} = 6.40$ yr. For the third cycle of instability shown in Figure 7(B3), $A = 61.3$ au, so $T_k = 0.95$, and $\Delta v_{\text{HP}} = v_H - v_p$ in g -direction is ~ 8.9 km s $^{-1}$, $\rho_i / \rho_o = 3.06$, so RT instability growth rate is $\gamma_{\text{RTI}} = 0.125$ and growth timescale is $1/\gamma_{\text{RTI}} = 8.03$ yr.

For the first cycle of instability shown in Figure 7(C1), $A = 56.4$ au, and $\Delta v_{\text{HP}} = v_H - v_p$ in N -direction is ~ 10.2 km s $^{-1}$,

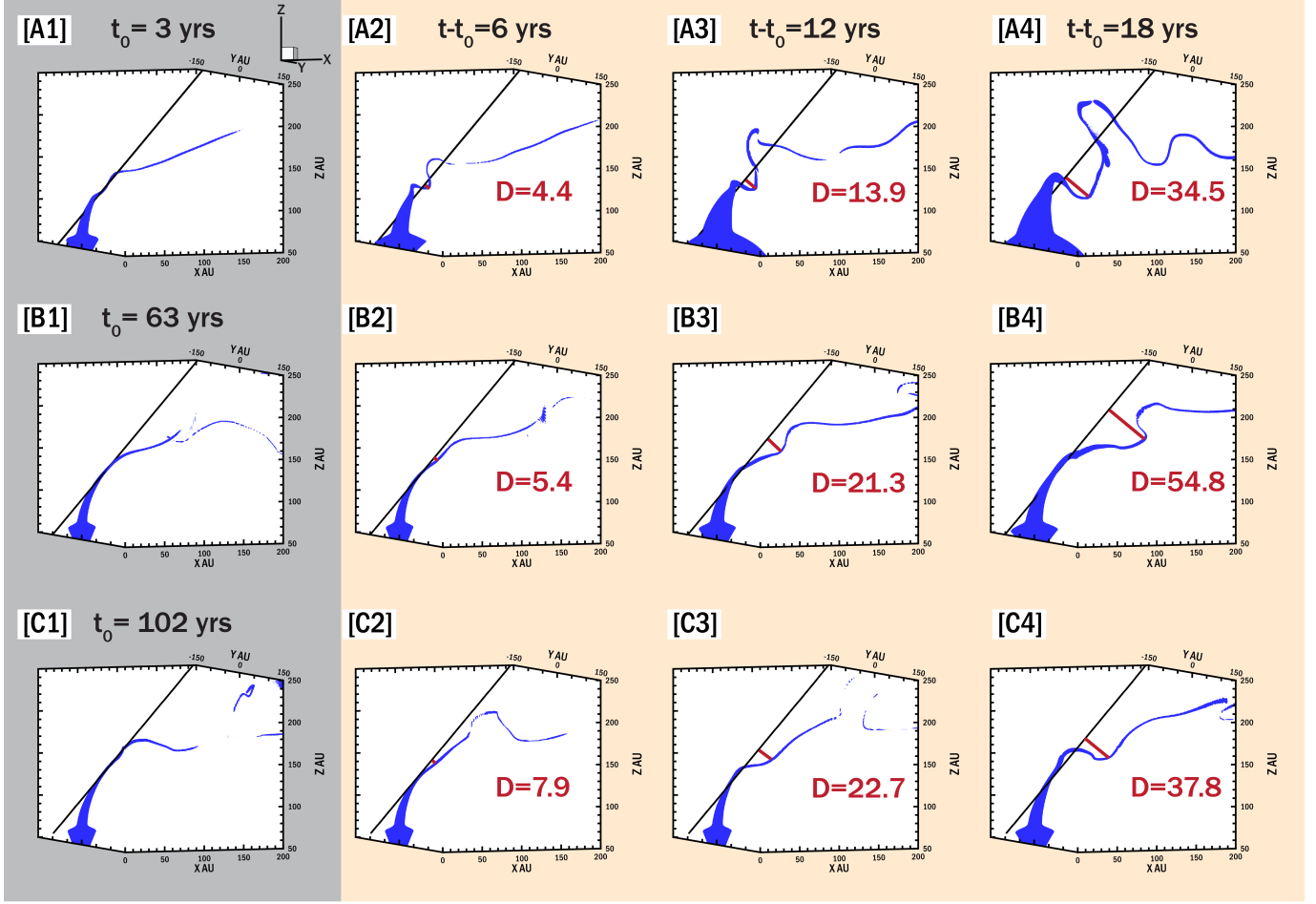


Figure 4. (A–C) The variation of displacement of instability structures from its initial position in the g -direction in the plane of the heliospheric jet over time at different initial times, with the blue isosurface representing $B = 0.05$ nT. The black lines indicate the initial position along the heliospheric jet axis, and the red lines represent the displacement (D) in the g -direction.

$\rho_i/\rho_o = 3.17$, so RT instability growth rate at initial time is $\gamma_{\text{RTI}} = 0.135$ and growth timescale is $1/\gamma_{\text{RTI}} = 7.41$ yr. As shown in Figure 7(C2), $A = 36.9$ au, and $\Delta v_{\text{HP}} = v_H - v_p$ in N -direction is ~ 8.06 km s $^{-1}$, $\rho_i/\rho_o = 8.62$, so RT instability growth rate at turning point time is $\gamma_{\text{RTI}} = 0.148$ and growth timescale is $1/\gamma_{\text{RTI}} = 6.76$ yr. For the third cycle of instability shown in Figure 7(C3), $A = 97.4$ au, and $\Delta v_{\text{HP}} = v_H - v_p$ in N -direction is ~ 7.21 km s $^{-1}$, $\rho_i/\rho_o = 2.84$, so RT instability growth rate at initial time is $\gamma_{\text{RTI}} = 0.109$ and growth timescale is $1/\gamma_{\text{RTI}} = 9.19$ yr. As shown in Figure 7(C4), $A = 52.7$ au, and $\Delta v_{\text{HP}} = v_H - v_p$ in N -direction is ~ 40.31 km s $^{-1}$, $\rho_i/\rho_o = 5.38$, so RT instability growth rate at turning point time is $\gamma_{\text{RTI}} = 0.174$ and growth timescale is $1/\gamma_{\text{RTI}} = 5.74$ yr.

For a finite shear layer width, the growth rate of KH instability can be calculated as $\gamma_{\text{KHI}} = \frac{\sqrt{\rho_i \rho_o}}{\rho_i + \rho_o} \cdot k_{\text{KHI}} \cdot \Delta U$ (S. Chandrasekhar 1961), where i, o means inside and outside of the slab, and ΔU is the speed difference, k is the wavenumber. It can be estimated from the scale length of the velocity shear, $k = \frac{1}{2a}$, where the scale length of the velocity shear $\nabla = 2a$ (A. Miura & P. L. Pritchett 1982). The shear scale length is defined as the distance from the central minimum to the points where the velocity equals the mean of its maximum and minimum values.

For the first cycle of instability shown in Figure 7(C1), since the velocity shear is symmetric in N -direction, $2\bar{\nabla} = 4a = 79.1$ au,

then $k_{\text{KHI}} = 0.025$ au $^{-1}$. From the solar wind velocity along the jet direction, we can get $U_i = 4.8$ km s $^{-1}$, $\bar{U}_o = 78.6$ km s $^{-1}$, then $\Delta U = 73.8$ km s $^{-1}$. $\rho_i/\rho_o = 3.17$, so KH instability growth rate in N -direction at initial time is $\gamma_{\text{KHI}} = 0.167$ and growth timescale is $1/\gamma_{\text{KHI}} = 5.97$ yr. As shown in Figure 7(C2), $2\bar{\nabla} = 4a = 117.2$ au, then $k_{\text{KHI}} = 0.017$ au $^{-1}$, $U_i = 10.1$ km s $^{-1}$, $\bar{U}_o = 77.5$ km s $^{-1}$, then $\Delta U = 67.4$ km s $^{-1}$. $\rho_i/\rho_o = 8.62$, so KH instability in N -direction growth rate at turning point time is $\gamma_{\text{KHI}} = 0.074$ and growth timescale is $1/\gamma_{\text{KHI}} = 13.55$ yr.

For the third cycle of instability shown in Figure 7(C1), since the velocity shear is symmetric in N -direction, $2\bar{\nabla} = 4a = 101.8$ au, then $k_{\text{KHI}} = 0.0196$ au $^{-1}$. From the solar wind velocity along the jet direction, we can get $U_i = 15.4$ km s $^{-1}$, $\bar{U}_o = 75.9$ km s $^{-1}$, then $\Delta U = 60.5$ km s $^{-1}$. $\rho_i/\rho_o = 2.84$, so KH instability growth rate in N -direction at initial time is $\gamma_{\text{KHI}} = 0.11$ and growth timescale is $1/\gamma_{\text{KHI}} = 9.11$ yr. As shown in Figure 7(C2), $2\bar{\nabla} = 4a = 118$ au, then $k_{\text{KHI}} = 0.0169$ au $^{-1}$, $U_i = 12.2$ km s $^{-1}$, $\bar{U}_o = 85.1$ km s $^{-1}$, then $\Delta U = 72.9$ km s $^{-1}$. $\rho_i/\rho_o = 5.38$, so KH instability in N -direction growth rate at turning point time is $\gamma_{\text{KHI}} = 0.10$ and growth timescale is $1/\gamma_{\text{KHI}} = 10.03$ yr.

When RT instability and KH instability are both present, the growth rate can be expressed as $\gamma_{\text{RTI+KHI}} = \gamma_{\text{RTI}}^2 + \gamma_{\text{KHI}}^2 = \sqrt{\alpha k_{\text{RTI}} g^* + \frac{\rho_i \rho_o}{(\rho_i + \rho_o)^2} k_{\text{KHI}}^2 \Delta U^2}$ (S. Chandrasekhar 1961). For the first instability cycle at the initial time, $\gamma_{\text{RTI+KHI}} = 0.215$,

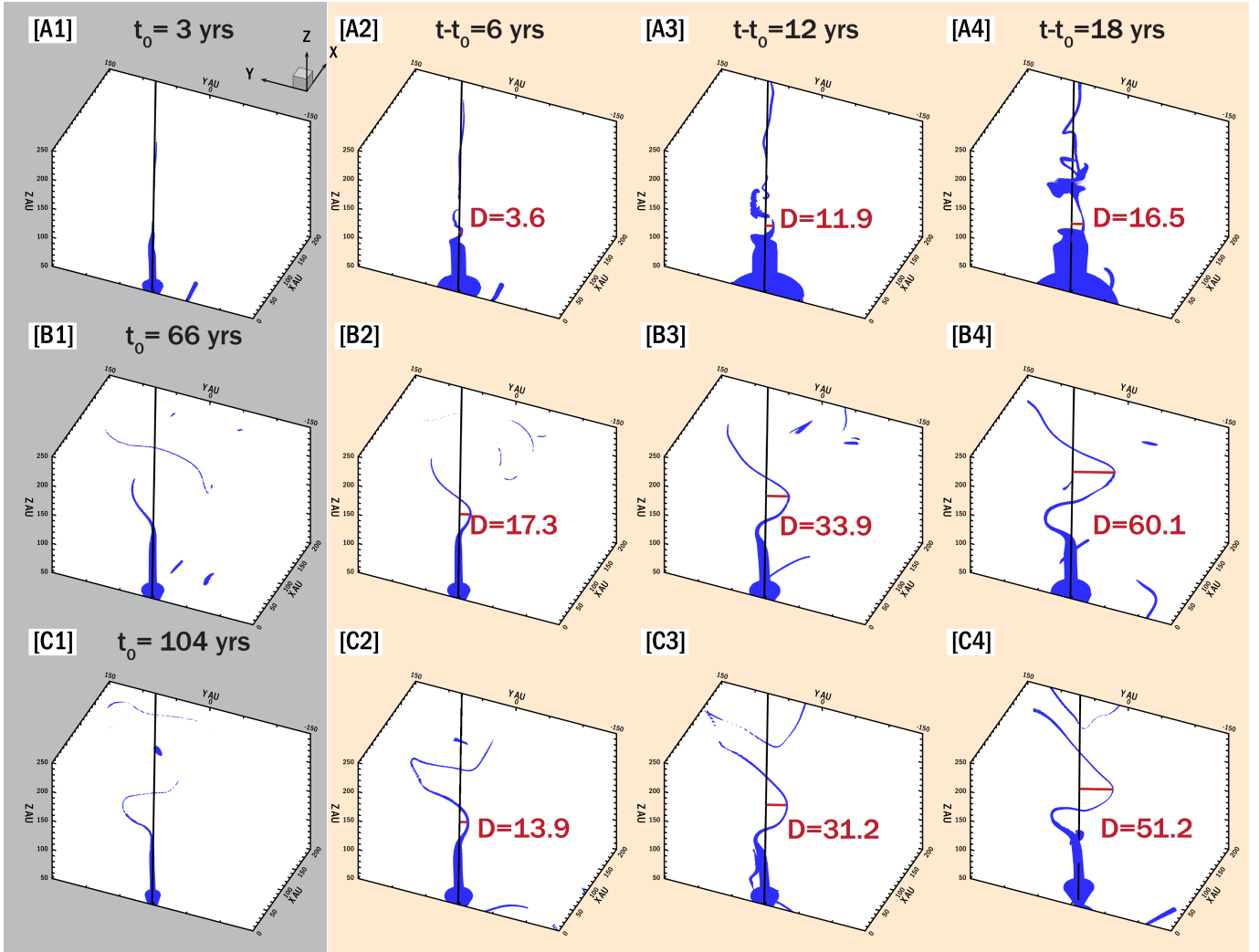


Figure 5. (A–C) The variation of displacement in the N -direction in the plane perpendicular to the plane of the heliospheric jet, intersecting it along the heliospheric jet direction. The blue isosurfaces represent $B = 0.05$ nT. The black lines indicate the initial position along the heliospheric jet axis, and the red lines represent the displacement (D) in the N -direction.

yielding a growth timescale of 4.65 yr. For the third cycle at the initial time, $\gamma_{\text{RTI+KHI}} = 0.155$, corresponding to a timescale of 6.47 yr (Figures 7(C2) and (C4)). As shown in Table 4, the combined growth timescales are comparable to the estimated growth rates from MHD simulations, suggesting that RT and KH instabilities initially evolve together in the N -direction. In the positive g -direction, Table 3 shows that the KH instability growth timescale is significantly longer than that of RT instability, due to the large width of the shear velocity profile (Figure 7(B)). Consequently, RT instability dominates in the positive g -direction.

After the turning point in the N -direction, the growth rates change. For the first cycle of instability, $\gamma_{\text{RTI+KHI}} = 0.165$ with a timescale of 6.05 yr. For the third cycle, $\gamma_{\text{RTI+KHI}} = 0.201$ with a timescale of 4.98 yr (Figures 7(C2) and (C4)). As indicated in Table 4, the estimated growth rate from the MHD model is lower than the theoretical combined growth rate but comparable to the growth timescale of KH instability alone. This suggests that RT and KH instabilities decouple during the later stages of evolution, reducing the overall instability timescale and forming a turning point in growth rate.

As shown in Figures 7(A1) and (A3), at the initial stage of each instability cycle, shear flows develop within the solar wind along the heliospheric jet, with velocity increasing outward from the axis. This velocity gradient leads to the generation of KH instability within the HS. As the instability evolves, both the solar wind density and velocity inside the HS undergo significant changes. As shown in Figures 7(A2) and (A4), the shear flow structure changes considerably. Near the center of the heliospheric jet, the solar wind speed becomes higher than the surrounding plasma, and as one moves outward from the axis, the velocity first decreases and then increases, forming a low-speed region with a ringlike structure along the jet.

In Figures 7(C2) and (C4), the solar wind velocity shear structure is no longer confined within the region where the density increases. This region is indicated by the green dashed lines. The solar wind density is constrained by the solar wind magnetic field, forming a density slab where RT instability develops. However, after a while, the instability structure extends beyond the high-density region. The estimated turning point of the instability growth lies outside the slab, marking a

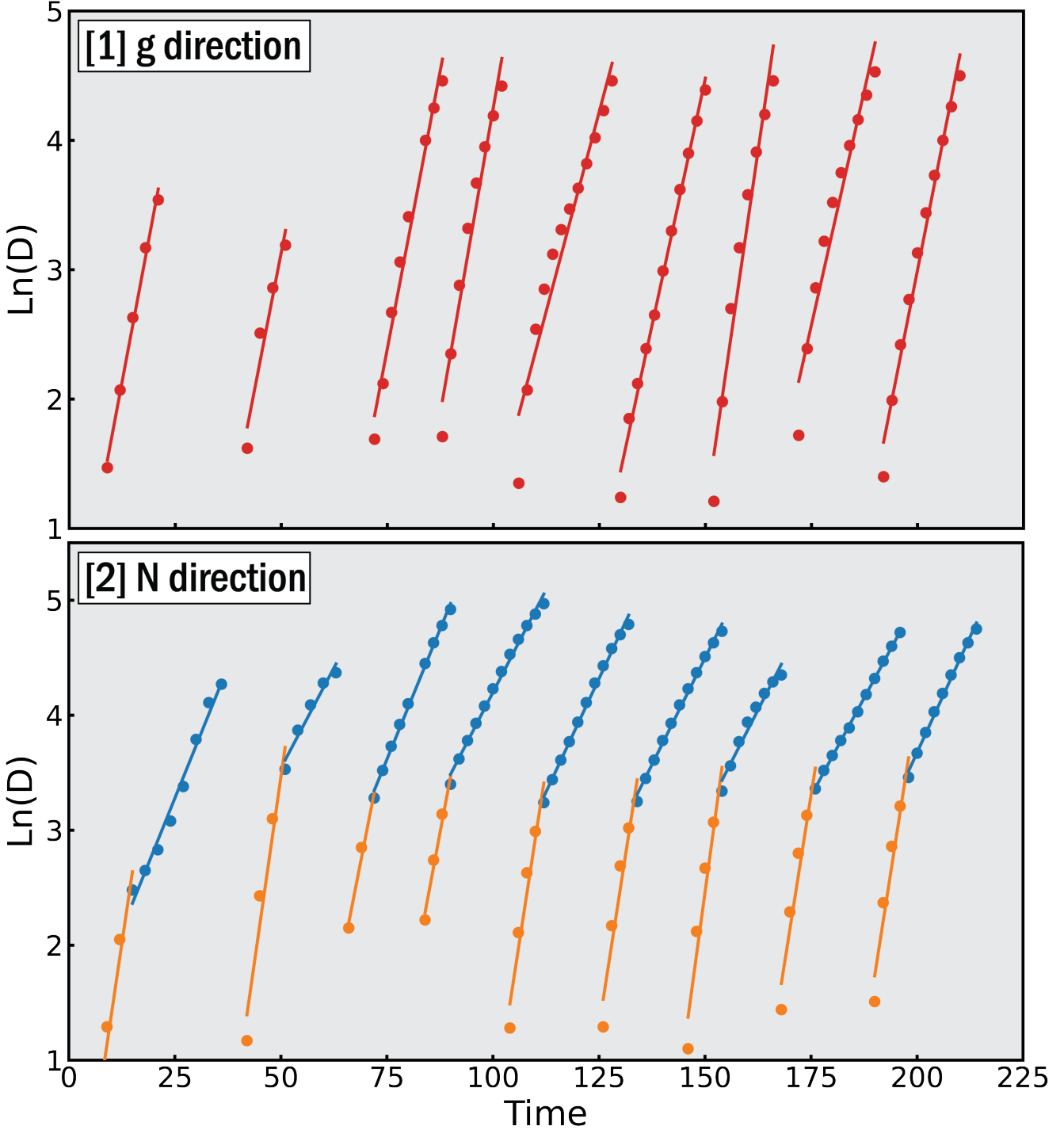


Figure 6. The time variation of the logarithm of displacement ($\ln D$) for each instability cycle in the g - and N -directions. (1) The red line represents the fitted trend for the measured data in the g -direction for each cycle. (2) In the N -direction, the orange lines correspond to the fitted data before the turning point in each cycle, while the blue lines represent the fit after the turning point.

transition where KH instability becomes dominant. Thus, in the N -direction, KH instability initially develops alongside RT instability but continues to grow independently, leading to a turning point in the instability growth rate.

4. Discussion and Conclusion

In this work, we run realistic ISM conditions with the interstellar magnetic field not perpendicular to the velocity of

the interstellar wind along the z -direction, but has an angle α_{BV} . These conditions tilt the plane of the heliospheric jet from the meridional plane, causing the effective gravity to have components both within the plane of the heliospheric jet (g -direction, perpendicular to the heliospheric axis) and normal to it (N -direction). RT instability is triggered by the effective gravitational force induced by charge-exchange interactions between solar wind ions and neutral H, and the

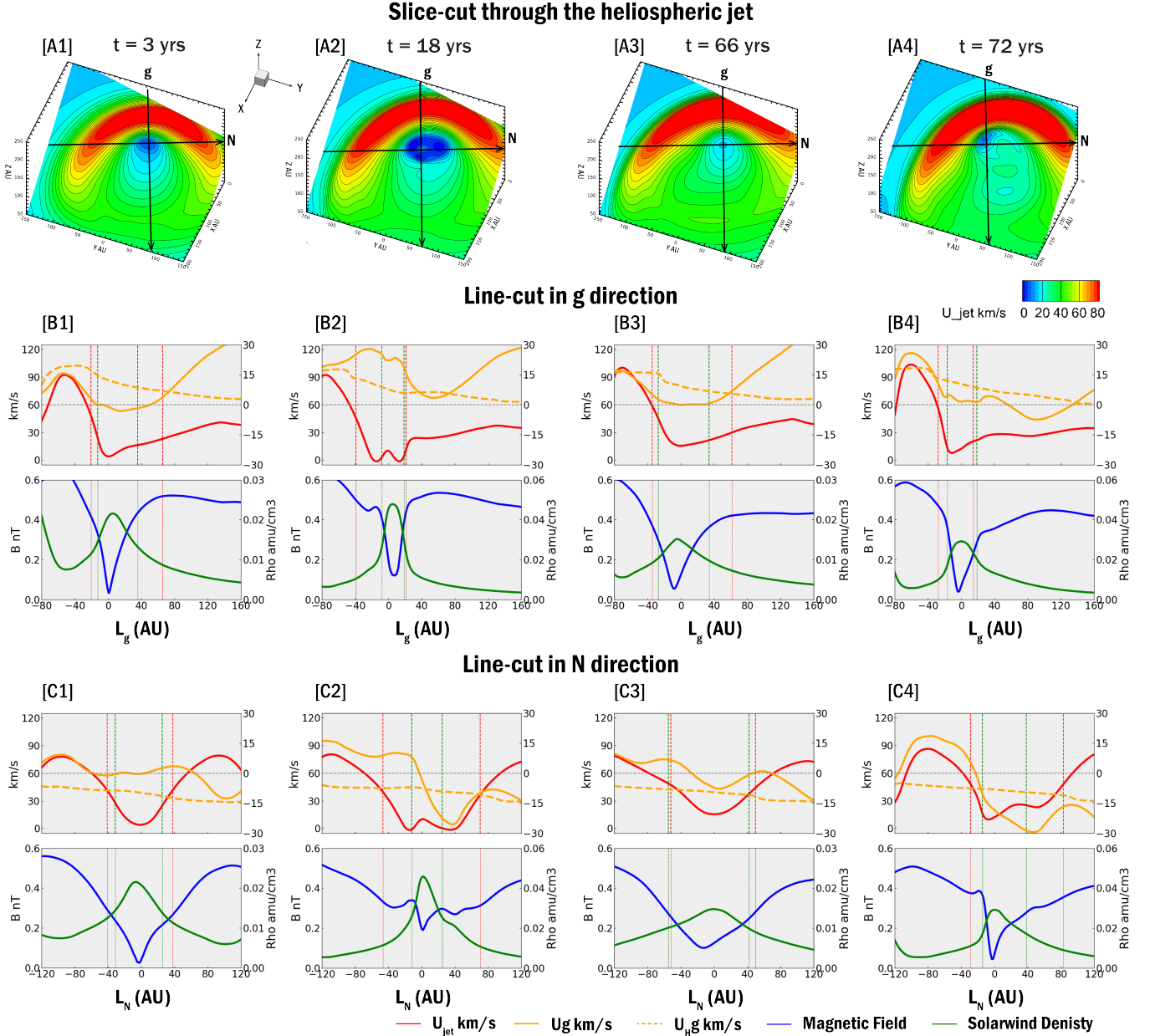


Figure 7. (A) The total solar wind speed in color contour on the cross section perpendicular to the heliospheric axis. (B) The solar wind density, total speed, speed along the g -direction, and neutral hydrogen speed along the g -direction along the line cut in the g -direction. (C) The solar wind density, total speed, speed along the N -direction, and neutral hydrogen speed along the N -direction along the line cut in the N -direction.

Table 1

Instability Growth Rate and Corresponding Timescale in the g -Direction for Each Cycle

Cycle	Initial Time t_0 (yr)	Growth Rate γ	Timescale $1/\gamma$ (yr)	R^2
1	3	0.175	5.7	0.99
2	39	0.169	5.9	0.93
3	63	0.172	5.8	0.98
4	82	0.189	5.3	0.96
5	102	0.123	8.1	0.94
6	126	0.152	6.6	0.99
7	146	0.227	4.4	0.96
8	166	0.145	6.9	0.95
9	188	0.167	6.0	0.98
Avg	...	0.169	5.9	...

shear flow induced by the low-speed region leads to the KH instability. With the 200 yr simulations, solar wind speed and magnetic field probed at a certain point show periodic fluctuations, revealing the dynamic evolution of the solar wind and magnetic field within the HS. These fluctuations arise alongside the development of RT and KH instabilities.

The MHD simulation results reveal that instabilities in the heliosheath occur periodically, with distinct growth rates in each cycle. In the g -direction, the average growth rate is approximately $\gamma = 0.169$, corresponding to a timescale of about 5.9 yr. In the N -direction, the instability growth rate is initially higher, averaging $\gamma = 0.234$ (corresponding to a timescale of ~ 4.2 yr), but decreases significantly after approximately 11.1 yr, forming a turning point at $\gamma = 0.077$, with an associated timescale of ~ 12.9 yr. This transition is

Table 2
Instability Growth Rate and Timescale in the N-Direction per Cycle

Cycle	Before the Turning Point				After the Turning Point				
	Initial Time t_0 (yr)	Growth Rate γ	Timescale $1/\gamma$ (yr)	R^2	Turning Point t_0 (yr)	Time to Turning Point (yr)	Growth Rate γ	Timescale $1/\gamma$ (yr)	R^2
1	3	0.250	4.0	0.96	18	15	0.091	11.0	0.98
2	39	0.256	3.9	0.94	51	12	0.069	14.4	0.95
3	63	0.189	5.3	0.98	72	9	0.090	11.1	1.00
4	82	0.196	5.1	0.98	90	8	0.071	14.0	0.99
5	102	0.238	4.2	0.95	112	10	0.079	12.7	0.99
6	126	0.238	4.2	0.93	134	8	0.074	13.5	0.95
7	146	0.270	3.7	0.93	154	8	0.072	13.9	0.97
8	166	0.233	4.3	0.94	176	10	0.068	14.7	1.00
9	188	0.238	4.2	0.94	198	10	0.081	12.4	0.99
Avg	...	0.234	4.2	11.1	0.077	12.9	...

Table 3
RT, KH, and Combined Instability Growth in the g -Direction

Cycle	Timescale of Instability: $1/\gamma$ (yr)			
	Theoretical		Theoretical RHI	Theoretical KHI and RTI
	MHD	KHI		
1	5.7	19.28	6.40	6.08
2	5.9	18.47	7.26	6.76
3	5.8	25.72	8.03	7.66
4	5.3	15.72	7.32	6.63
5	8.1	28.11	7.67	7.40
6	6.6	30.57	8.04	7.77
7	4.4	18.56	8.12	7.44
8	6.9	26.61	8.15	7.79
9	6.0	25.50	8.39	7.97
Avg	6.0	23.98	7.48	7.32

Table 4
RT, KH, and Combined Instability Growth in the N -Direction

Cycle	1/ γ (yr) Before the Turning Point				1/ γ (yr) After the Turning Point			
	MHD	Theoretical KHI	Theoretical RHI	Theoretical KHI and RTI	MHD	Theoretical KHI	Theoretical RHI	Theoretical KHI and RTI
1	4.0	5.97	7.41	4.65	11.0	13.55	6.76	6.05
2	3.9	7.90	6.66	5.09	14.4	10.09	5.47	4.81
3	5.3	9.11	9.19	6.47	11.1	10.03	5.74	4.98
4	5.1	7.84	8.96	5.90	14.0	15.21	4.80	4.57
5	4.2	8.29	9.62	6.28	12.7	10.94	5.51	4.92
6	4.2	9.46	17.60	8.33	13.5	10.68	5.53	4.91
7	3.7	8.76	9.56	6.46	13.9	13.84	5.02	4.72
8	4.3	8.83	11.09	6.91	14.7	14.08	4.93	4.65
9	4.2	9.06	9.76	6.64	12.4	12.37	4.78	4.46
Avg	4.2	8.46	9.13	6.17	12.9	12.02	5.38	4.79

attributed to the simultaneous presence of RT and KH instabilities.

In the N -direction, RT and KH instabilities initially evolve together, but as the instability develops, they decouple. This is due to significant changes in the solar wind density and velocity structure inside the HS, where a low-speed region transforms into a ringlike structure around the heliospheric jet axis. As the instability structure extends beyond the density slab, where RT instability grows, KH instability grows

independently, leading to a decrease in the overall growth rate after the turning point. In the positive g -direction, the growth timescale of KH instability is much longer than that of RT instability, owing to the broader shear velocity profile in this direction. This suggests that RT instability is the primary instability mechanism in the g -direction.

Therefore, our results suggest that these two instabilities can evolve together and develop periodically. This coevolution not only enhances the complexity of the system but also plays a

potentially crucial role in shaping the large-scale structure of the heliosphere, especially the formation of open tail regions. As the instabilities transition from their linear to nonlinear growth phases, they become capable of inducing significant turbulence and enhancing particle transport and acceleration. These nonlinear effects are essential features of the open tail configuration. Therefore, RT and KH instabilities may represent a fundamental mechanism initiating the first stage of tail opening and restructuring in the outer heliosphere.

To better understand the global impact of these processes, future studies will focus on the downstream regions of the heliosphere, particularly the heliotail. By analyzing the evolution of instabilities downward to the heliotails, we aim to uncover their influence on the turbulence generation and the open tails. Such investigations are crucial for forming a comprehensive picture of heliosphere structure.

This study uses a single-fluid plasma model, combining cold thermal solar wind and hot pickup ions (PUIs) into one fluid. However, advanced models like M. Opher et al. (2020) treat these populations separately and show that PUI depletion cools and “deflates” the heliosphere, leading to a narrower heliosheath and a more rounded shape. Since PUIs significantly affect the heliospheric structure, they may also influence the formation of the low-speed region and the development of instabilities along heliospheric jets. Future work will adopt multifluid models to investigate how these instabilities are affected by the separation of cooler thermal solar wind ions and the hotter PUIs. Meanwhile, future work may also adopt time-dependent models to explore how the dynamic behavior of instabilities evolves in response to solar-cycle-driven changes in the heliosphere.

Acknowledgments

The authors were supported by NASA grant 18-DRIVE18_2-0029, Our Heliospheric Shield, 80NSSC22M0164, and FINESST award 20-HELI020-0009, The structure of the heliosphere and heliotail with a Multi-ion and Kinetic Neutrals treatment. Resources supporting this work were provided by the NASA High-End Computing (HEC) program through the NASA Advanced Supercomputing (NAS) Division at Ames Research Center. The authors would like to thank the staff at NASA Ames

Research Center for the use of the Pleiades supercomputer under the award SMD-20-46872133.

ORCID iDs

Xiaohan Ma [ID](https://orcid.org/0000-0003-0007-757X) <https://orcid.org/0000-0003-0007-757X>
 Merav Opher [ID](https://orcid.org/0000-0002-8767-8273) <https://orcid.org/0000-0002-8767-8273>
 Marc Kornbleuth [ID](https://orcid.org/0000-0002-3479-1766) <https://orcid.org/0000-0002-3479-1766>

References

- Avinash, K., Zank, G., Dasgupta, B., & Bhadaria, S. 2014, *ApJ*, **791**, 102
- Avinash, K., Zank, G., Dasgupta, B., & Bhadaria, S. 2015, *JPhCS*, **577**, 012002
- Baranov, V., Fahr, H. J., & Ruderman, M. 1992, *A&A*, **261**, 341
- Baranov, V. B., Krasnobaev, K. V., & Ruderman, M. S. 1976, *Ap&SS*, **41**, 481
- Begelman, M. C. 1998, *ApJ*, **493**, 291
- Chalov, S. V. 1996, *A&A*, **308**, 995
- Chandrasekhar, S. 1961, *Hydrodynamic and Hydromagnetic Stability* (New York: Oxford Univ. Press)
- Chen, Y., Toth, G., Powell, E., et al. 2024, *ApJ*, **973**, 46
- Drake, J. F., Swisdak, M., & Opher, M. 2015, *ApJL*, **808**, L44
- Florinski, V., Zank, G. P., & Pogorelov, N. V. 2005, *JGRA*, **110**, A07104
- Fraternale, F., Pogorelov, N. V., & Bera, R. K. 2023, *ApJ*, **946**, 97
- Golikov, E. A., Izmodenov, V. V., Alexashov, D. B., & Belov, N. A. 2016, *MNRAS*, **464**, 1065
- Izmodenov, V., & Alexashov, D. 2015, *ApJS*, **220**, 32
- Kornbleuth, M., Opher, M., Baliukin, I., et al. 2021, *ApJ*, **923**, 179
- Liewer, P., Karmesin, S., & Brackbill, J. 1996, *JGR*, **101**
- Lindsay, B., & Stebbings, R. 2005, *JGRA*, **110**, A12213
- Ma, X., Opher, M., Kornbleuth, M., & Toth, G. 2024, *ApJ*, **978**, 57
- Michael, A. T., Opher, M., Toth, G., Tenishev, V., & Borovikov, D. 2022, *ApJ*, **924**, 105
- Miura, A., & Pritchett, P. L. 1982, *JGR*, **87**, 7431
- Opher, M., Bibi, F. A., Toth, G., et al. 2009, *Natur*, **462**, 1036
- Opher, M., Drake, J. F., Zank, G., et al. 2021, *ApJ*, **922**, 181
- Opher, M., Drake, J. F., Zieger, B., & Gombosi, T. I. 2015, *ApJL*, **800**, L28
- Opher, M., Liewer, P. C., Gombosi, T. I., et al. 2003, *ApJL*, **591**, L61
- Opher, M., Loeb, A., Drake, J., & Toth, G. 2020, *NatAs*, **4**, 675
- Parker, E. N. 1958, *ApJ*, **128**, 664
- Parker, E. N. 1961, *ApJ*, **134**, 20
- Pogorelov, N. V., Borovikov, S. N., Heerikhuisen, J., & Zhang, M. 2015, *ApJL*, **812**, L6
- Tóth, G., van der Holst, B., Sokolov, I. V., et al. 2012, *JCoPh*, **231**, 870
- Yu, G. 1974, *ApJ*, **194**, 187
- Zank, G. P. 1999, *SSRv*, **89**, 413
- Zank, G. P., Pauls, H. L., Williams, L. L., & Hall, D. T. 1996, *JGRA*, **101**, 21639